Real-time absorption and scattering characterization of slab-shaped turbid samples obtained by a combination of angular and spatially resolved measurements

Jan S. Dam, Nazila Yavari, Søren Sørensen, and Stefan Andersson-Engels

We present a fast and accurate method for real-time determination of the absorption coefficient, the scattering coefficient, and the anisotropy factor of thin turbid samples by using simple continuous-wave noncoherent light sources. The three optical properties are extracted from recordings of angularly resolved transmittance in addition to spatially resolved diffuse reflectance and transmittance. The applied multivariate calibration and prediction techniques are based on multiple polynomial regression in combination with a Newton–Raphson algorithm. The numerical test results based on Monte Carlo simulations showed mean prediction errors of approximately 0.5% for all three optical properties within ranges typical for biological media. Preliminary experimental results are also presented yielding errors of approximately 5%. Thus the presented methods show a substantial potential for simultaneous absorption and scattering characterization of turbid media.

OCIS codes: 170.3890, 170.7050.

1. Introduction

The optical properties,[1] i.e., the absorption coefficient μ_a, the scattering coefficient μ_s, and the anisotropy factor g, of a turbid (i.e., multiple-scattering) medium can provide important information on the composition and the dynamics of the medium. Whereas μ_a renders information on the concentration of various chromophores,[2,3] μ_s and g provide information on the form, size, and concentration of the scattering components in the medium.[4,5] Thus accurate and fast determination of μ_a, μ_s, and g of turbid media is useful and important in numerous fields of science and medicine, as well as industry and environmental monitoring. Some examples are tissue characterization in cancer diagnostics and therapy,[6] medical diagnostics with biological fluids,[7] and process control in breweries and dairies.[8,9] However, most existing methods for optical analysis of turbid media are not able to extract μ_a, μ_s, and g simultaneously and many methods also focus on either the absorption or the scattering properties, i.e., the scattering effects are treated as interference during absorption measurements[9,10] or vice versa.[11,12] Yet other methods rely on removal of the scattering components prior to absorption measurements, e.g., some types of clinical blood analysis[13,14] where the blood cells are hemolyzed (the cell walls are crushed) and subsequently removed from the sample either by means of sedimentation or centrifugation.

Integrating sphere (IS) measurements[15–17] are widely used as a reference method for determination of μ_a, μ_s, and g for relatively thin turbid samples. Here, the optical properties are extracted from measurements of the total diffuse reflectance R_{tot} and the total diffuse transmittance T_{tot} of either a solid slab or a suspension in a cuvette. IS measurements may be carried out using a single- or a double-sphere setup. In the latter case, R_{tot} and T_{tot} can be recorded simultaneously without moving the sample; but because of optical cross talk between the two spheres, the accuracy is normally decreased compared with a single-sphere setup. Still, only μ_a and the reduced scattering

J. S. Dam, N. Yavari, and S. Andersson-Engels (stefan.andersson-engels@fysik.lth.se) are with the Department of Physics, Lund Institute of Technology, P.O. Box 118, SE-22100 Lund, Sweden. N. Yavari is also with the Department of Physics and Technology, Bergen University, Allégaten 55, N-5007 Bergen, Norway. S. Sørensen is with Bang & Olufsen Medicom, DK-7600 Struer, Denmark.

Received 25 October 2004; revised manuscript received 24 February 2005; accepted 25 February 2005.

0003-6935/05/204281-10$15.00/0

coefficient $\mu_s' = (1 - g)\mu_s$ can be determined from pure R_{tot} and T_{tot} measurements. To separate μ_s' into μ_s and g it is necessary to perform additional measurements of the collimated transmittance T_c in a separate setup, i.e., the sample has to be moved once again. Moreover, it is complicated to perform accurate T_c measurements in practice; thus IS-based methods are applied mainly for research purposes. Methods for simultaneous extraction of μ_a, μ_s, and g based on angularly resolved transmittance measurements have also been suggested[18]; however, these methods also typically involve complex instrumentation.

In summary, the existing methods for determination of optical properties from thin turbid samples either imply more or less accurate interference compensation techniques, bulky equipment, inconvenient sample handling, or technically complicated measurements. Hence, there is an obvious need for more compact, handy, and accurate techniques for this type of measurements.

In the following we present a novel method for real-time simultaneous determination of μ_a, μ_s, and g from slab-shaped turbid samples using continuous-wave (i.e., steady-state) light sources. We first describe the geometric configuration of the setup and the principles of the applied multivariate calibration and prediction techniques, which are based on the so-called multiple polynomial regression (MPR)[17] in conjunction with a Newton–Raphson (N-R) algorithm.[19] Then, using Monte Carlo (MC) simulated data,[20] we show how the optical properties can be determined from four (or less) combined recordings of the angularly resolved transmittance, the spatially resolved diffuse transmittance, and the spatially resolved diffuse reflectance of the sample. Finally, we present preliminary experimental results obtained from measurements on a set of solid epoxy phantoms and from measurements on a series of milk samples.

2. Methods

As stated above, the purpose of the research described in this paper is to extract μ_a, μ_s, and g from recordings of various combinations of angularly and spatially resolved reflected and transmitted intensities from a slab-shaped turbid sample using multivariate calibration.

A. Geometric Configuration

The basic geometric configuration of the setup used for the analyses in this paper is shown in Fig. 1. The setup models a cuvette with sample thickness d_s = 1.0 mm, wall thickness d_w = 1.0 mm, and collimated beam diameter d_b = 1.0 mm. The refractive indices of the sample n_s, the wall n_w, and the surrounding media n_m are 1.33, 1.49, and 1.00, respectively. Recordings of the spatially resolved diffuse reflectance and transmittance from the cuvette are denoted as R and T, respectively, whereas various recordings of the angularly resolved transmittance are denoted as α_i, where $i = 1, 2, \ldots$.

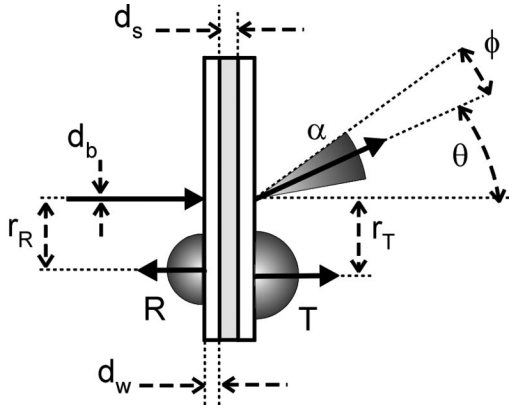

Fig. 1. Geometric configuration of setup for measuring μ_a, μ_s, and g, where R and T are the spatially resolved diffuse reflectance and transmittance, respectively, with radial distance r. The angularly resolved transmittance is denoted as α, where θ is the deflection angle and ϕ is the acceptance angle. Finally, d_s is the sample thickness, d_b is the diameter of the collimated source beam, and d_w is the thickness of the cuvette walls.

Figure 2 shows the schematics of the four different R, T, and α configurations that we investigate in this paper. In Fig. 2(a), μ_a, μ_s, and g are predicted from three angular recordings, α_1, α_2, and α_3. In Fig. 2(b), μ_s and g are predicted from two angular recordings, α_1 and α_2. Figure 2(c) is used to predict μ_a and μ_s' from two spatial recordings, R and T. Finally, in Fig. 2(d), a combination of the recordings in Figs. 2(b) and 2(c), i.e., α_1, α_2, R, and T, is applied to extract μ_a, μ_s, and g.

B. Monte Carlo Simulations

To investigate the optical property prediction performances of the four configurations shown in Fig. 2, a series of MC simulations based on the geometry specified in Fig. 1 was carried out.[20] Thus, in each single MC simulation, R and T were recorded as a function of the radial distance r_T and r_R, respectively, and α_i

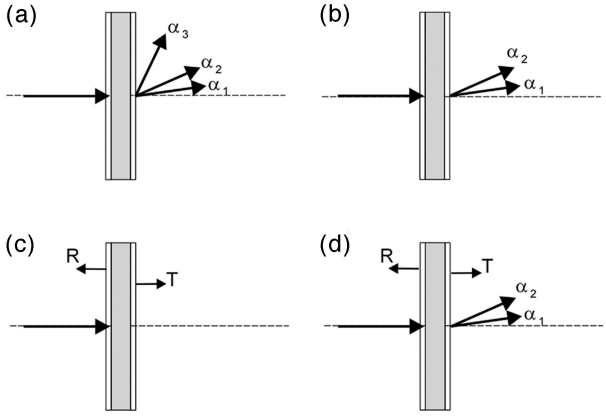

Fig. 2. Four different setups used to predict optical properties with various combinations of spatially or angularly resolved data. Each single setup can be used for determination of (a) μ_a, μ_s, and g; (b) μ_s and g; (c) μ_a and μ_s'; (d) μ_a, μ_s, and g. See Fig. 1 for nomenclature.

was recorded as a function of the deflection angle θ and the acceptance angle ϕ. In each case, r_T and r_R varied within the ranges 0–10 mm in steps of 0.1 mm, whereas θ varied within the range 0°–90° in steps of 0.25°.

The scored recordings of R, T, and α were obtained and stored in a $21 \times 19 \times 11$ calibration matrix, i.e., a database containing all combinations of 21 values of μ_a, 19 values of μ_s, and 11 values of g within the typical biological ranges[21]:

$$0 < \mu_a < 2 \text{ cm}^{-1},$$

$$10 < \mu_s < 200 \text{ cm}^{-1},$$

$$0.85 < g < 0.99. \tag{1}$$

Previous research[17] using similar analysis methods in conjunction with IS measurements showed relative errors <1% between the calculated calibration models and the actual MC simulated model based on 10^6 photon packets within typical biological ranges of μ_a and μ_s'. Preliminary investigations in this work showed similar results regarding the stochastic noise of the MC simulations. Thus the calibration matrix applied throughout this paper was generated using 10^6 photon packets in each single case. Note that this does not imply that the calibration models might be off by ~1% in some cases, as the applied MPR calibration algorithms effectively smoothen out any random fluctuations caused by the stochastic nature of the MC simulations.

C. Multivariate Calibration and Prediction

To provide a calibration model for the subsequent prediction analyses, the so-called MPR was applied on the MC simulated recordings of R, T, and α stored in the $21 \times 19 \times 11$ calibration matrix. Preliminary tests with third-, fourth-, and fifth-order polynomials showed that third-order polynomials yielded the highest accuracy and stability; thus third-order polynomials were used for all analyses in this paper. The exact MPR algorithm applied depends on the specific configuration in question, i.e., Figs. 2(a), 2(b), 2(c), or 2(d). In the following, the configuration in Fig. 2(a) will serve to illustrate the general principles of the applied MPR algorithm. First a subset of the $21 \times 19 \times 11$ calibration matrix was rearranged into a $I \times J$ matrix, where I is the number of samples used (i.e., $I = 4389 = 21 \times 19 \times 11$) and J is the number of applied variables, i.e., $J = 3$ in this case:

$$\begin{bmatrix} \alpha_{1,1} & \alpha_{1,2} & \alpha_{1,3} \\ \alpha_{2,1} & \alpha_{2,2} & \alpha_{2,3} \\ \cdots & \cdots & \cdots \\ \alpha_{I,1} & \alpha_{I,2} & \alpha_{I,3} \end{bmatrix} = \begin{bmatrix} g_1(\mu_{a,1}, \mu_{s,1}, g_1) & g_2(\mu_{a,1}, \mu_{s,1}, g_1) & g_3(\mu_{a,1}, \mu_{s,1}, g_1) \\ g_1(\mu_{a,2}, \mu_{s,2}, g_2) & g_2(\mu_{a,2}, \mu_{s,2}, g_2) & g_3(\mu_{a,2}, \mu_{s,2}, g_2) \\ \cdots & \cdots & \cdots \\ g_1(\mu_{a,I}, \mu_{s,I}, g_I) & g_2(\mu_{a,I}, \mu_{s,I}, g_I) & g_3(\mu_{a,I}, \mu_{s,I}, g_I) \end{bmatrix}. \tag{2}$$

Here, $\alpha_{i,1}$, $\alpha_{i,2}$, and $\alpha_{i,3}$ are the recorded angularly resolved transmittance [see Figs. 1 and 2(a)], and the functions g_1, g_2, and g_3 are triple polynomials defined as

$$g_1(\mu_a, \mu_s, g) = \sum_{k=0}^{M} \sum_{l=0}^{M} \sum_{q=0}^{M} a_{klq} \mu_a{}^k \mu_s{}^l g^q,$$

$$g_2(\mu_a, \mu_s, g) = \sum_{k=0}^{M} \sum_{l=0}^{M} \sum_{q=0}^{M} b_{klq} \mu_a{}^k \mu_s{}^l g^q,$$

$$g_3(\mu_a, \mu_s, g) = \sum_{k=0}^{M} \sum_{l=0}^{M} \sum_{q=0}^{M} c_{klq} \mu_a{}^k \mu_s{}^l g^q. \tag{3}$$

Accordingly, a_{klq}, b_{klq}, and c_{klq} are the fitting (or calibration) coefficients determined by least-squares regression, and M is the order of the polynomials (i.e., $M = 3$ in this paper).

The next step is to solve the inverse problem of determining μ_a and μ_s' from recorded prediction data sets, i.e., sets of $[\alpha_{1,\text{meas}}\ \alpha_{2,\text{meas}}\ \alpha_{3,\text{meas}}]$ with unknown values of μ_a, μ_s, and g. First we define

$$F(\mu_a, \mu_s, g) = g_1 - \alpha_{1,\text{meas}},$$

$$G(\mu_a, \mu_s, g) = g_2 - \alpha_{2,\text{meas}},$$

$$H(\mu_a, \mu_s, g) = g_3 - \alpha_{3,\text{meas}}, \tag{4}$$

where g_{1-3} are defined by Eqs. (3). Then we use a N-R algorithm [Eqs. (5)] to perform converging iterative calculations of μ_a, μ_s, and g:

$$-\begin{bmatrix} F(\mu_{a,k}, \mu_{s,k}, g_k) \\ G(\mu_{a,k}, \mu_{s,k}, g_k) \\ H(\mu_{a,k}, \mu_{s,k}, g_k) \end{bmatrix} = \begin{bmatrix} \frac{\partial F}{\partial \mu_a} & \frac{\partial F}{\partial \mu_s} & \frac{\partial F}{\partial g} \\ \frac{\partial G}{\partial \mu_a} & \frac{\partial G}{\partial \mu_s'} & \frac{\partial G}{\partial g} \\ \frac{\partial H}{\partial \mu_a} & \frac{\partial H}{\partial \mu_s'} & \frac{\partial H}{\partial g} \end{bmatrix} \begin{bmatrix} h_{a,k} \\ h_{s,k} \\ h_{g,k} \end{bmatrix}$$

$$\begin{bmatrix} \mu_{a,k+1} \\ \mu_{s,k+1} \\ g_{k+1} \end{bmatrix} = \begin{bmatrix} \mu_{a,k} \\ \mu_{s,k} \\ g_k \end{bmatrix} + \begin{bmatrix} h_{a,k} \\ h_{s,k} \\ h_{g,k} \end{bmatrix}$$

$$k = 0, 1, 2, 3, \ldots, \tag{5}$$

where h_a, h_s, and h_g are the correction terms of μ_a, μ_s, and g, respectively. The calculations continue until h_a, h_s, and h_g have dropped below predefined maximum values (i.e., in this paper, $h < 10^{-6}$).

In Fig. 2(b) we have two variables only, i.e., α_1 and α_2. Consequently, only two optical properties, i.e., μ_s and g, are applied in the algorithms of Eqs. (2)–(5). In turn, the three triple polynomials $g_{1\text{–}3}(\mu_a, \mu_s, g)$ in Eq. (2) are replaced by two double polynomials $g_{1\text{–}2}(\mu_s, g)$, and the dimensions of the matrices and functions in the subsequent Eqs. (3)–(5) are changed accordingly. Likewise, during the analyses of Fig. 2(c) only R and T are recorded. Thus only μ_a and μ_s' and double polynomials of the form $g(\mu_a, \mu_s')$ are applied in the algorithms of Eqs. (2)–(5). Such two-variable MPR techniques have been described in detail in some of our previous work on IS measurements and analyses.[17] In Fig. 2(d) we have four variables ($J = 4$). Since the MPR–N-R method implies exactly three variables to predict μ_a, μ_s, and g, we have to apply some sort of dimension reduction. For this we use the principal component analysis (PCA),[22] that is, we perform PCA on the $I \times 4$ calibration matrix and then use the resulting three main principal components to create a new $I \times 3$ matrix as input to the calibration and prediction algorithms described by Eqs. (2)–(5). By applying PCA here, we expect that any relevant information on the relationship between $[R\ T\ \alpha_1\ \alpha_2]$ and $[\mu_a\ \mu_s\ g]$ in the calibration data set will be concentrated in the three main principal components and that any embedded noise, e.g., stochastic MC noise, will be isolated in the fourth principal component, which is then discarded during calibration and prediction.

D. Phantom and Milk Sample Measurements

To support the presented numerical results we also performed preliminary experiments using measurements on solid epoxy phantoms[23] and milk samples. These experiments were carried out using a laboratory setup based on the geometry shown in Fig. 2(d). In this case, the thickness of the samples d_s was 1.0 mm; the radial distances r_R and r_T were 2.5 and 2.0 mm, respectively; and the angles α_1 and α_2 were 0° and 5°, respectively. Furthermore, a He–Ne laser (633 nm) with a beam diameter d_b of 1.0 mm was used as a light source. Optical fibers were used to collect the output signals from the setup. These fibers were connected to a set of silicon detectors with matching amplifier electronics mounted in a breakout box. This box was connected to a data-acquisition PC card controlled by LabVIEW software.

3. Results

All the prediction errors that we report in this section are mean errors relative to the total optical property ranges of the applied prediction test data.

A. Numerical Tests

To test the performance of the four configurations in Fig. 2, we first generated a set of MC simulated prediction data with 20 random combinations of optical properties within the ranges:

$$0 < \mu_a < 2\ \text{cm}^{-1},$$

$$50 < \mu_s < 100\ \text{cm}^{-1},$$

$$0.85 < g < 0.95. \quad (6)$$

All prediction data were generated with 10^7 photons. Table 1 shows the results from the prediction tests by use of these data in conjunction with the four configurations in Fig. 2. In each case the prediction errors were minimized using error plots similar to Fig. 3, i.e., the applied angles α or distances r in each of the four configurations represent the combinations of α and r values yielding minimal overall prediction errors. Table 2 shows the optimal angles and the distances corresponding to the errors listed in Table 1. The μ_s range of the above prediction data [inequalities (6)] covers only a part of the range spanned by the calibration model [inequalities (1)]. To test the performance of the prediction algorithms on a wider range of the calibration model, we generated two additional test sets with μ_a and g ranges similar to inequalities (6), but with the following μ_s ranges: $(10 < \mu_s < 50\ \text{cm}^{-1})$ and $(100 < \mu_s < 150\ \text{cm}^{-1})$, respectively. The prediction errors for all three μ_s ranges are given in Table 3.

Table 1. Mean Prediction Errors from the Analyses on the Four Configurations in Fig. 2 at Optimal Settings for R, T, α_1, and α_2

	Mean Prediction Errors (%)			
Configuration	μ_a	μ_s	g	μ_s'
Fig. 2(a)	0.83	0.47	0.68	—
Fig. 2(b)	—	0.95	3.9	—
Fig. 2(c)	0.84	—	—	0.23
Fig. 2(d)	0.17	0.45	0.43	—

In some cases, the sample thickness $d_s = 1.0$ mm of the applied calibration model may be too large for proper prediction at large μ_a and μ_s values (see Table 3). A calibration model with a smaller d_s may of course solve this problem. Another solution is to employ the technique of scaling both the optical coefficients and the sample thickness.[24] This will enable use of the original calibration data (with $d_{s,\text{org}} = 1.0$ mm) on samples with $d_{s,\text{new}} < 1.0$ mm by multiplying the predicted μ_a and μ_s values with the scaling factor $s = d_{s,\text{org}}/d_{s,\text{new}}$. Figure 4 shows the resulting correlation plots of true and scaled predicted values of μ_a, μ_s, and g when prediction data with $d_{s,\text{new}} = 0.5$ mm are used as input to the original calibration model with $d_{s,\text{org}} = 1.0$ mm.

Dividing a large calibration data set into smaller subsets may improve the overall accuracy. Thus, by splitting the prediction data in Fig. 4 into three μ_s subranges [indicated by the dashed lines in Fig. 4(b)] and applying three separate calibration submodels as well, the mean of the μ_a and g prediction errors dropped from 2.2% to 0.59% and from 0.59% to 0.26%,

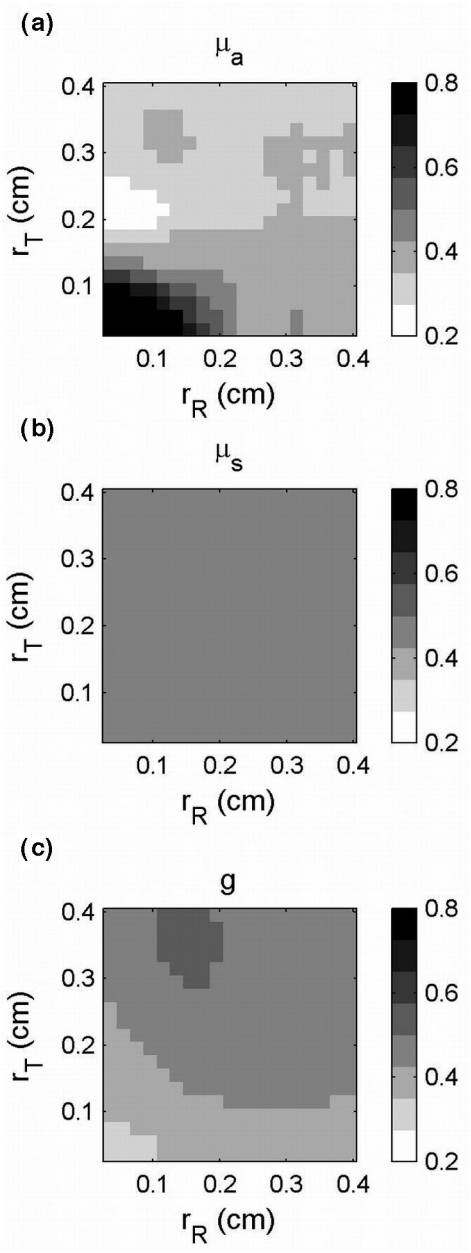

Fig. 3. Prediction errors of (a) μ_a, (b) μ_s, and (c) g as a function of r_T and r_R with the setup of Fig. 2(d) in conjunction with a prediction data set defined by inequalities (6). The deflection angles of α_1 and α_2 were 0° and 5°, respectively.

Table 2. Optimum Angles and Distances of the Four Configurations in Fig. 2

	Angles θ (deg)			Distances r (mm)	
Configuration	α_1	α_2	α_3	T	R
Fig. 2(a)	0	3	60	—	—
Fig. 2(b)	0	3	—	—	—
Fig. 2(c)	—	—	—	0.7	2.0
Fig. 2(d)	0	5	—	2.0	2.5

Table 3. Prediction Errors for Various μ_s Ranges from the Configuration of Fig. 2(d)

	Mean Prediction Errors (%)		
Varying μ_s Ranges	μ_a	μ_s	g
$10 < \mu_s < 50$ cm^{-1}	1.7	0.10	0.28
$50 < \mu_s < 100$ cm^{-1}	0.17	0.45	0.43
$100 < \mu_s < 150$ cm^{-1}	8.6	36	14

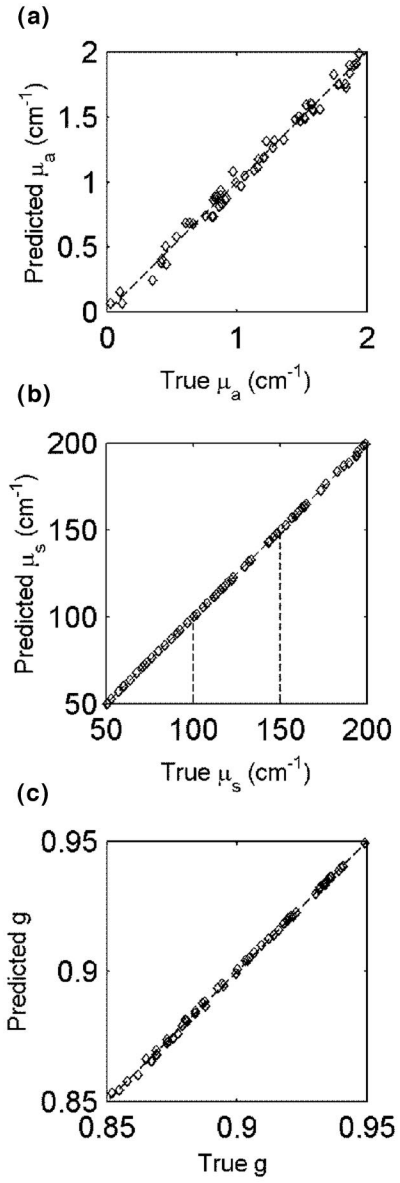

Fig. 4. Predicted values of (a) μ_a, (b) μ_s, and (c) g as a function of the true values obtained with the setup of Fig. 2(d) (d_s = 1.0 mm) in conjunction with downscaled prediction data (d_s = 0.5 mm). The corresponding prediction errors of μ_a, μ_s, and g are 2.2, 0.40, and 0.59%, respectively. The dashed lines in (b) indicate the μ_s ranges of three subsets of calibration and prediction data. The resulting μ_a, μ_s, and g prediction errors obtained from these subranges are 0.59, 0.58, and 0.26%, respectively.

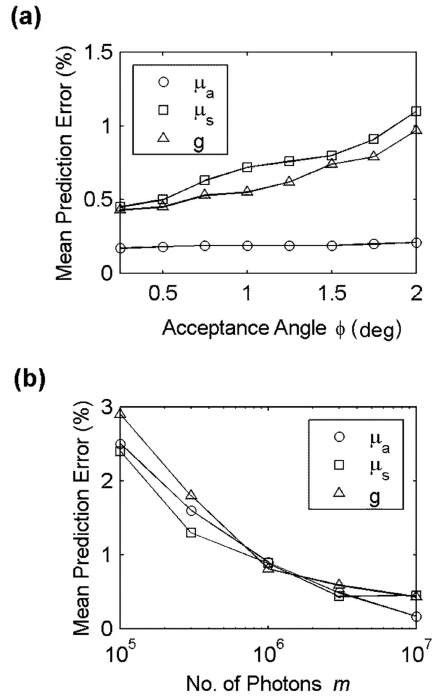

Fig. 5. Prediction errors of μ_a, μ_s, and g as a function of (a) the acceptance angle ϕ_a of α_1 and (b) the number of photons used to generate the prediction data. The optical property ranges of the prediction data are in both cases defined by inequalities (6), and $d_s = 1.0$ mm.

respectively. However, the μ_s prediction error also showed a slight increase, rising from 0.40% to 0.58%.

During the analysis of the data in Table 1, the acceptance angles of α_2 and α_3, i.e., ϕ_2 and ϕ_3, both were 1°, and the acceptance angles of α_1 and ϕ_1 was 0.25°. Such a relatively small acceptance angle may be difficult to implement in practice; thus Fig. 5(a) shows the prediction errors of μ_a, μ_s, and g as a function of ϕ_1. Noise is another problem encountered during real measurements. To illustrate the effect of random noise in the prediction data set, Fig. 5(b) shows the prediction errors of μ_a, μ_s, and g as a function of the applied number of photons m for five otherwise similar prediction sets. The optical property ranges for the prediction data in both Fig. 5(a) and 5(b) are given by inequalities (6).

B. Experimental Results

Figure 6 shows the prediction results from the epoxy phantom measurements. As it is shown the prediction errors of μ_a and μ_s' are 5.9% and 3.0%, respectively. The reference values of the 25 epoxy phantoms were determined using an IS setup as described in a previous paper.[23] The g factor of the applied epoxy phantoms was almost constant ($g \sim 0.75$); thus we performed prediction analyses of μ_a and μ_s' only. Because of the inherent difficulties in reproducing the exact geometry of the measurement setup in the MC simulations, we chose to base the prediction analysis on the so-called leave-one-out cross-validation tests performed directly on the 25 phantoms, i.e., the prediction of μ_a and μ_s' of a single phantom in the 25 phantom set was carried out using a calibration model generated from the μ_a and μ_s' reference values of the remaining 24 phantoms. To ensure a proper calibration model range we included predictions on the inner 9 phantoms of the 25 phantoms only, as indicated in Fig. 6. Several analyses with various combinations of measured R, T, α_1, and α_2 data were performed, both with and without applying PCA. However, it turned out that in this particular case a combination of R and α_1 data solely provided the best prediction results for μ_a and μ_s'.

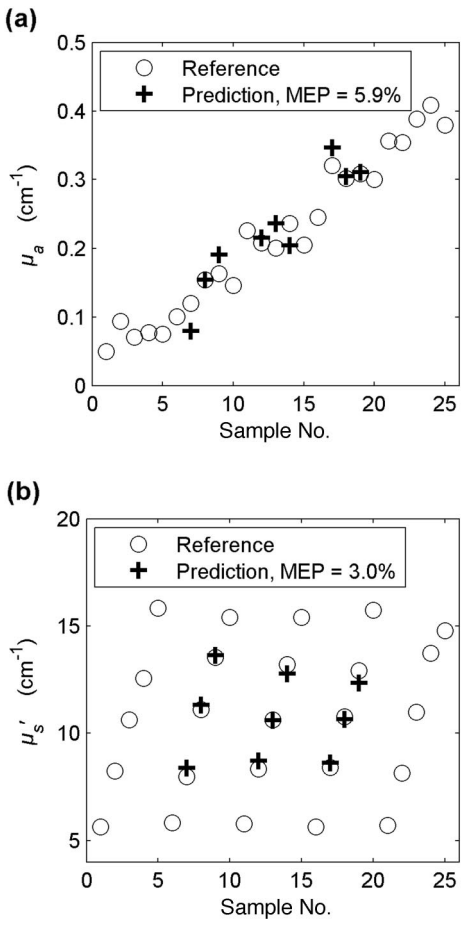

Fig. 6. Experimental prediction results of μ_a and μ_s' based on R and α_1 measurements on epoxy phantoms. The reference values of the phantoms were determined using an IS setup.[23] MEP, mean error of prediction.

To assess how the measurement setup handled biological and liquid samples and how such measurements compared with MC simulations, we also carried out a series of measurements on milk samples with varying water contents in a flow cuvette. At the time, it was not possible to obtain reference values of μ_a, μ_s', and g for the milk samples, so the investigations were limited to the inspection of the raw T, α_1, and α_2 data shown in Figs. 7(a) and 7(b). Note that the measured R data had to be discarded subsequently because of a faulty detector. The indicated fat percentage of the diluted milk samples in Fig. 7(a)

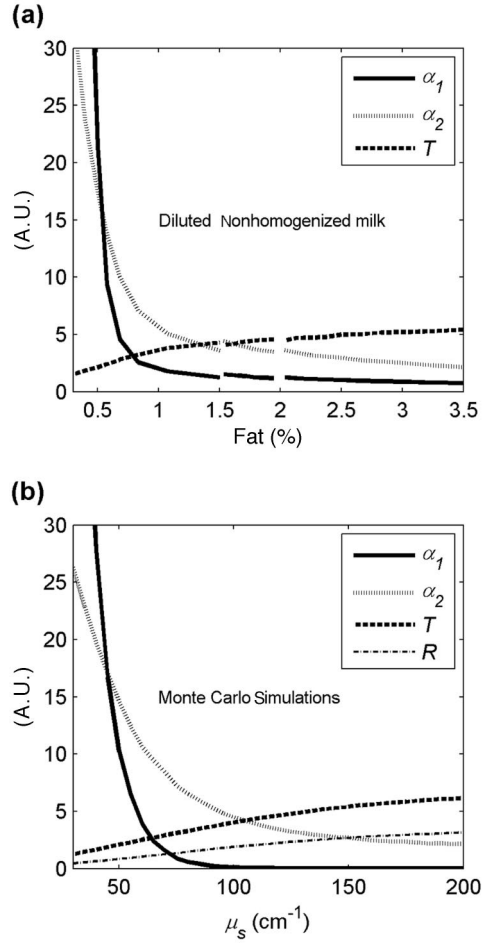

Fig. 7. (a) Measured and (b) MC simulated R, T, α_1, and α_2 data. The measurements were carried out on milk samples with varying water contents in a flow cuvette, and the MC data were extracted from the calibration set defined by inequalities (1). Note that the R data in (a) were discarded because of a faulty detector.

was calculated on the basis of the fat content stated by the dairy; furthermore, multiple series of natural and low-fat milk with water added were used, hence the gaps of the curves in Fig. 7(a). Since reference values of μ_a, μ_s', and g for the milk samples were not available, numerous MC simulations with combinations of μ_a and g from the MC calibration set [inequalities (1)] were examined by visual inspection. As illustrated in Fig. 7(b), it appeared that MC simulations based on μ_a and g values of 0.1 cm^{-1} and 0.94, respectively, showed a good resemblance with the milk sample measurements.

4. Discussion

A. Optimum Setup

The results in Table 1 show that it is possible to predict μ_a, μ_s, and g with errors less than 1% using the purely angularly resolved configuration of Fig. 2(a). However, the relatively large optimum angle of α_3 ($\theta_{\alpha_3} = 60°$) in this configuration, may be inconvenient to implement in real applications. Thus, in a search for a more feasible geometric configuration, we tested the configurations in Figs. 2(b) and 2(c) as well. Figure 2(c) was chosen because of its similarity to the IS measurements, hence we also chose to perform prediction tests on μ_a in combination with μ_s' instead of μ_s. The results in Table 1 show that both μ_a and μ_s' can be predicted with good accuracy using this setup. Now that we were able to perform an accurate determination of μ_a and μ_s', the next step was to find a feasible geometric configuration for accurate determination of either μ_s or g. Then it would be possible, in principle, to determine all three optical properties by combining the two configurations. On the basis of our experience with Fig. 2(a), we chose to apply Fig. 2(b) for the μ_s and g prediction tests. From Table 1 it appears that at least μ_s may be predicted with good accuracy using this configuration, while the prediction accuracy of g is moderate. Still, according to the above considerations, we required only the prediction of μ_s or g to be accurate; thus we finally combined Figs. 2(b) and 2(c) finally leading to the hybrid configuration in Fig. 2(d).

Figure 2(d) obviously has four output variables, i.e., α_1, α_2, T and R. Because the applied MPR–N-R algorithms imply exactly three variables to determine the three requested optical properties, i.e., μ_a, μ_s, and g, we chose to apply the PCA to reduce the dimension of the variables from four to three. In short, the PCA procedure extracts the relevant information in a set of calibration variables and generates a new set of variables, the so-called principal components, i.e., PC_1, PC_2, and so on, which are sorted according to their respective variances. As a result, almost all information on μ_a, μ_s, and g from α_1, α_2, T, and R is embedded in PC_{1-3}, whereas a major part of the random noise from the MC simulations are isolated in PC_4, which is disregarded during calibration and prediction. As a bonus, use of the PCA thus decreases the noise sensitivity of the applied prediction methods, i.e., the robustness of the method is increased.

Initially, we performed prediction tests on Fig. 2(d) using the optimal angles and distances found during the analysis of Figs. 2(b) and 2(c) (see Table 2). This also yielded good results, but the short optimal distance of T ($r_t = 0.7$ mm) may be difficult to implement if goniometric measurements at α_1 and α_2 are to be performed simultaneously. We therefore carried out the error analysis depicted in Fig. 3. The results showed that there is no need for a meticulous selection of r_T and r_R in Fig. 2(d) as long as $1.5 < [r_T\, r_R] < 3.0$ mm, where the lower limit was determined by the prediction errors of μ_a and the upper limit by the prediction errors of g. It also appeared that the prediction errors of μ_s was practically invariant in the range $0 < [r_T\, r_R] < 4$ mm. The results depicted in Fig. 3 are based on $\theta_{\alpha_1} = 0°$ and $\theta_{\alpha_2} = 5°$. We carried out similar analyses for the range $1° < \theta_{\alpha_2} < 10°$ as well. The results showed that the prediction accuracy of all three optical properties were practically independent of θ_{α_2} in this range. Because of these loose restrictions on the geometric configuration of α_1, α_2, T, and R, the configuration in Fig. 2(d) appears to be relatively sim-

ple and straightforward to implement. As a consequence, we based all further analyses on this configuration using the values of θ_{α_1}, θ_{α_2}, r_T, and r_R listed in Table 2 [for Fig. 2(d)]. Table 3 shows that the prediction performance of Fig. 2(d) is good in the lower and the middle μ_s ranges. Still, the prediction error of μ_a in the lower μ_s range is significantly larger than the other errors. This may be due to the fact that the calibration model was optimized for the middle range. Moreover, the analyses on Figs. 2(b) and 2(c) suggest that the information on μ_a, to a large extent, is embedded in the spatially resolved recordings of R and T. Thus, if $\mu_s = 10\ \text{cm}^{-1}$, this, statistically speaking, leads to one single-scattering event if the sample thickness $d_s = 1.0$ mm. Consequently, only a few photons will be recorded at $r_T = 2.0$ mm and $r_R = 2.5$ mm, leading to a poor prediction of μ_a. In this case it may be advantageous to apply a larger d_s. The prediction accuracy of the upper μ_s range in Table 3 is inadequate. Here, a large sample thickness in conjunction with large μ_s values lead to an almost complete diffuse transmittance, i.e., it is difficult to extract any information on μ_s and g from the goniometric recordings of α_1 and α_2, which in turn makes it difficult to determine μ_a as well. In this case it may be advantageous to decrease d_s.

B. Model Scaling

As discussed above, the sample thickness $d_s = 1.0$ mm may be too large for proper prediction of large values of μ_s. As mentioned in the results above, this problem may be solved by applying a calibration model and prediction data with a smaller d_s. However, in some cases, it may be too tedious to generate a new calibration model. Therefore we tried to feed downscaled prediction data, i.e., $d_s = 0.5$ mm, to the original calibration model ($d_s = 1.0$ mm) and then subsequently correct the results by multiplying the predicted μ_a and μ_s by 2. During such a procedure, it is important to remember that r_T, r_R, and d_b of the prediction data have to be scaled as well, in opposition to the α data, which are invariant to any scaling of d_s. The results given in Fig. 4 show a good prediction accuracy for μ_a, μ_s, and g, although the μ_s range is substantially wider than, e.g., the individual tests reported in Table 3. Still, the prediction error of $\mu_a = 2.2\%$ may be unacceptable in some cases. However, as stated above this error may be substantially reduced by splitting the calibration model used in Fig. 4 into three submodels. As a trade-off, the prediction error of μ_s is slightly increased, probably owing to the reduced μ_s resolution of the three calibration submodels compared with the full-range model. Thus, in real applications that demand high accuracy and wide optical property ranges, a two-step prediction algorithm might be advantageous. This could be implemented by first making a rough estimate of μ_a, μ_s, and g and then subsequently zoom in on the relevant submodel to perform a second more accurate prediction of μ_a. In summary, the results in Fig. 4 actually suggest that a calibration model with $d_s = 0.5$ mm would be a better choice as a general-purpose model for the optical property ranges defined by inequalities (1) than the model with $d_s = 1.0$ mm that we started out with.

C. Acceptance Angle and Noise Considerations

During the analysis leading to the results in Table 3, the acceptance angle ϕ_1 was 0.25°. Because such a relatively small angle may be difficult to implement in some applications, we carried out a series of prediction tests with varying ϕ_1. The results from these tests are shown in Fig. 5(a). It appears that the prediction error of μ_a is unaffected by the changes in ϕ_1 and that the prediction errors of both μ_s and g increase more or less linearly as function of ϕ_1. This agrees well with the above discussions regarding the optimum setup, which suggest that μ_a is mainly determined from the R and T data, as opposed to μ_s and g, which are mainly determined from α_1 and α_2. The increase in the errors of μ_s and g is most likely due to the fact that, when ϕ_1 increases, so does the probability that the recorded photons may have been scattered twice or more and still be within the limits of ϕ_1. In other words, two (or more) scattering events may be misinterpreted as a single-scattering event leading to incorrect values of μ_s and g. However, the results in Fig. 5(a) also show that ϕ_1 may be increased to at least 2° without any serious reduction of the overall prediction accuracy. In light of the practical problems encountered during T_c measurements in connection with IS measurements, this result is interesting, because it is a considerably simpler task to perform α_1 measurements with a finite acceptance angle ($\phi_1 \sim 1°$) than T_c measurements with $\phi_1 = 0°$. But the above discussion also suggests that predictions made with Fig. 2(d) on data with large g values may cause problems. Thus we tested our method on a set of prediction data with μ_a and μ_s ranges similar to inequalities (6), but with a wider g range, i.e., $0.9 < g < 0.98$. The results showed prediction errors $<0.7\%$ for all three optical properties. This leads to the conclusion that our method may be extended to include at least $g \leq 0.98$ without any serious effect on the overall performance.

As mentioned above, noise is another practical problem encountered during real measurements. The decay of the prediction errors shown in Fig. 5(b) agrees well with the theoretical $P_{\text{noise}} \propto (1/m)^{0.5}$ relation between the random MC noise P_{noise} and the number of applied photons m. Furthermore, it appears that all three errors have dropped below 1% already at $m = 10^6$. These results only stress the importance of minimizing the noise sources during real measurements.

D. Phantom and Milk Measurements

The experimental prediction errors of μ_a and μ_s' of the epoxy phantoms (i.e., 3.0% and 5.9%) are considerably larger than the errors found in the numerical tests (~0.5%). This is somewhat to be expected partly because of the difficulties in reproducing the exact

geometric configuration of the MC simulations in an experimental setup and partly because of the introduced measurement noise and inhomogeneous samples. In addition, the reference data in this analysis were provided by an IS setup, i.e., the references themselves are probably not completely accurate. Furthermore, the calibration models used in the experimental tests were much less detailed (24 samples) than the models of the numerical tests (~4000 samples), which in turn also leads to less accurate models.

The α_1, α_2, and T plots in Figs. 7(a) and 7(b) show a distinct resemblance between the measured data and the MC simulated data; however, minor deviations can be observed. These deviations might also be contributed to slight differences in the geometric configuration of the measurement setup and the MC simulations. But it should also be noted that the concentration of any chromophore in the milk (e.g., protein and lactose) will also vary as a function of the water added, i.e., μ_a and not only μ_s may vary in Fig. 7(a), as opposed to the MC simulations of Fig. 7(b), where μ_a is kept constant on two estimated values, i.e., 0.1 cm^{-1} and 0.94, respectively.

When the sample thickness $d_s = 1.0$ mm as in this case, it is not possible to perform accurate predictions if $\mu_s > 100$ cm^{-1} (see Table 3). Thus, from the results in Fig. 7, it can be concluded that, to properly analyze milk with a natural fat content (3%–5%), it is necessary to apply a cuvette with a smaller d_s, e.g., 0.5 mm.

5. Conclusions

We have developed a novel method for accurate real-time determination of the optical properties μ_a, μ_s, and g from spatially and angularly resolved measurements on slab-shaped turbid samples, i.e., solid slabs or liquid samples in a cuvette.

The method has been tested both numerically using Monte Carlo simulated data and experimentally using epoxy phantoms and milk samples. In general, the results showed a good correlation between the Monte Carlo simulations the experimental results, as we also have demonstrated in some of our previous work.[17,25]

However, whereas the numerical tests yielded typical prediction errors of 0.5%, the phantom experiments yielded somewhat larger errors of 3%–6%. Still, prediction errors of 3%–6% based on data from real measurements are not discouraging and the errors could probably be further minimized using larger and more detailed calibration data sets in conjunction with an improved next-generation instrumentation. Such instrumentation is especially interesting because of its obvious advantages compared with integrating-sphere-based methods, e.g., (a) the sample does not have be moved during the measurements, i.e., real-time analysis is possible; (b) no bulky spheres are needed; and (c) no technically complicated collimated transmittance measurements are required.

Thus we are confident that it is feasible to implement the presented method in compact and cost-effective practical instrumentation maintaining a prediction performance adequate for a variety of applications.

The authors acknowledge financial support from the Danish Academy of Technical Sciences, the European Commission Molecular Imaging Programme (2002-LIFESCIHEALTH-503259).

References

1. A. J. Welch, M. J. C. van Gemert, W. M. Star, and B. C. Wilson, "Overview of tissue optics," in *Optical-Thermal Response of Laser-Irradiated Tissue*, A. J. Welch and M. J. C. van Gemert, eds. (Plenum, 1995), pp. 15–46.
2. J. W. Feather, D. J. Ellis, and G. Leslie, "A portable reflectometer for the rapid quantification of cutaneous haemoglobin and melanin," Phys. Med. Biol. **33,** 711–722 (1988).
3. S. L. Jacques, "Reflectance spectroscopy with optical fiber devices and transcutaneous bilirubinometers," in *Biomedical Optical Instrumentation and Laser-Assisted Biotechnology*, A. M. Verga Scheggi, S. Martellucci, A. N. Chester, and R. Pratesi, eds. (Kluwer Academic, 1996), pp. 83–94.
4. J. R. Mourant, J. P. Freyer, A. H. Hielscher, A. A. Eick, D. Shen, and T. M. Johnson, "Mechanisms of light scattering from biological cells relevant to noninvasive optical-tissue diagnostics," Appl. Opt. **37,** 3586–3593 (1998).
5. S. L. Jacques, "Origins of tissue optical properties in the UVA, visible, and NIR regions," in *Advances in Optical Imaging and Photon Migration*, R. R. Alfano and J. G. Fujimoto, eds., Vol. 2 of OSA Trends in Optics and Photonics Series (Optical Society of America, 1996), pp. 364–369.
6. A. M. K. Nilsson, R. Berg, and S. Andersson-Engels, "Measurements of the optical properties of tissue in conjunction with photodynamic therapy," Appl. Opt. **34,** 4609–4619 (1995).
7. A. Roggan, M. Friebel, K. Dörschel, A. Hahn, and G. Müller, "Optical properties of circulating human blood in the wavelength range 400–2500 nm," J. Biomed. Opt. **4,** 36–46 (1999).
8. S. R. Kamath, C. V. Morr, and T. Schenz, "Laser light scattering and microscopic properties of milkfat globules in Swiss cheese whey low density lipid-containing fraction," Lebensm.-Wiss. Technol. **31,** 274–278 (1998).
9. Y. Woo, Y. Terazawa, J. Y. Chen, C. Iyo, F. Terada, and S. Kawano, "Development of a new measurement unit (MilkSpec-1) for rapid determination of fat, lactose, and protein in raw milk using near-infrared transmittance spectroscopy," Appl. Spectrosc. **56,** 599–604 (2002).
10. H. Martens and R. Steiner, "Extended multiplicative signal correction and spectral interference subtraction: new preprocessing methods for near infrared spectroscopy," J. Appl. Physiol. **9,** 625–635 (1991).
11. H. Schnablegger and O. Glatter, "Sizing of colloidal particles with light scattering: corrections for beginning multiple scattering," Appl. Opt. **34,** 3489–3501 (1995).
12. A. A. Kokhanovsky and R. Weichert, "Multiple light scattering in laser particle sizing," Appl. Opt. **40,** 1507–1513 (2001).
13. M. Peake, B. Mazzachi, A. Fudge, and R. Bais, "Bilirubin measured on a blood gas analyser: a suitable alternative for near-patient assessment of neonatal jaundice?" Ann. Clin. Biochem. **38,** 533–540 (2001).
14. B. Rolinski, H. Küster, B. Ugele, R. Gruber, and K. Horn, "Total bilirubin measurement by photometry on a blood gas analyzer: potential for use in neonatal testing at the point of care," Clin. Chem. **47,** 1845–1847 (2001).

15. J. W. Pickering, S. A. Prahl, N. van Wieringen, J. F. Beek, H. J. C. M. Sterenborg, and M. J. C. van Gemert, "Double-integrating-sphere system for measuring the optical properties of tissue," Appl. Opt. **32,** 399–410 (1993).
16. A. N. Yaroslavsky, I. V. Yaroslavsky, T. Goldbach, and H. J. Schwarzmaier, "Influence of the scattering phase function approximation on the optical properties of blood determined from the integrating sphere measurements," J. Biomed. Opt. **4,** 47–53 (1998).
17. J. S. Dam, T. Dalgaard, P. E. Fabricius, and S. Andersson-Engels, "Multiple polynomial regression method for determination of biomedical optical properties from integrating sphere measurements," Appl. Opt. **39,** 1202–1209 (2000).
18. S. Willmann, H. J. Schwarzmaier, A. Terenji, I. V. Yaroslavsky, and P. Hering, "Quantitative microspectrophotometry in turbid media," Appl. Opt. **38,** 4904–4913 (1999).
19. S. V. Chapra and R. P. Canale, *Numerical Methods for Engineers* (McGraw-Hill, 1997).
20. L. Wang, S. L. Jacques, and L. Zheng, "MCML-Monte Carlo modeling of light transport in multi-layered tissues," Comput. Methods Programs Biomed. **47,** 131–146 (1995).
21. W. F. Cheong, S. A. Prahl, and A. J. Welch, "A review of the optical properties of biological tissue," IEEE J. Quantum Electron. **26,** 2166–2185 (1990).
22. J. E. Jackson, "Principal component and factor analysis: Part I. Principal components," J. Quality Technol. **12,** 201–213 (1980).
23. J. Swartling, J. S. Dam, and S. Andersson-Engels, "Comparison of spatially and temporally resolved diffuse-reflectance measurement systems for determination of biomedical optical properties," Appl. Opt. **42,** 4612–4620 (2003).
24. A. Pifferi, P. Taroni, G. Valentini, and S. Andersson-Engels, "Real-time method for fitting time-resolved reflectance and transmittance measurements with a Monte Carlo model," Appl. Opt. **37,** 2774–2780 (1998).
25. J. S. Dam, C. B. Pedersen, T. Dalgaard, P. Aruna, and S. Andersson-Engels, "Fiber-optic probe for noninvasive real-time determination of tissue optical properties at multiple wavelengths," Appl. Opt. **40,** 1155–1164 (2001).